Thermodynamically Controlled Self-Assembly of Hierarchically Staggered Architecture as an Osteoinductive Alternative to Bone Autografts

Yan Liu,* Dan Luo, Min Yu, Yu Wang, Shanshan Jin, Zixin Li, Shengjie Cui, Danqing He, Ting Zhang, Tie Wang,* and Yanheng Zhou*

Osteoinductive synthetic biomaterials for replacing autografts can be developed by mimicking bone hierarchy and surface topography for host cell recruitment and differentiation. Until now, it has been challenging to reproduce a bone-like staggered hierarchical structure since the energy change underlying synthetic pathways in vitro is essentially different from that of the natural process in vivo. Herein, a bone-like hierarchically staggered architecture is reproduced under thermodynamic control involving two steps: fabrication of a high-energy polyacrylic acid-calcium intermediate and selective mineralization in collagenous gap regions driven by an energetically downhill process. The intermediate energy interval could easily be adjusted to determine different mineralization modes, with distinct morphologies and biofunctions. Similar to bone autografts, the staggered architecture offers a bone-specific microenvironment for stem cell recruitment and multidifferentiation in vitro, and induces neo-bone formation with bone marrow blood vessels by host stem cell homing in vivo. This work provides a novel perspective for an in vitro simulating biological mineralization process and proof of concept for the clinical application of smart biomaterials.

1. Introduction

Natural bone is a dynamic, highly vascularized tissue that contains a mineralized matrix with a hematopoietic bone marrow in the central cavities, and provides mechanical support, physical protection, and mineral storage site for the mammalian body.[1] Massive bone defects resulting from trauma or excision of large bone segments constitute a great challenge to reconstructive surgery.[2] Autologous bone is still the golden standard for bone regeneration, for its osteoconductive ability to guide the in-growth of osteoblasts and osteoinductive capability to induce bone formation by stimulating osteogenic differentiation of local stem cells, which is essential for the repair of large critical-sized bone defects.[3,4] Drawbacks of autografting including the limited supply and donor site morbidity make the preparation of osteoinductive biomaterials as autograft substitutes an area of intense research.[3,4] The currently used bone substitutes such as calcium-phosphate ceramics and mineralized collagen composites try to simulate the mineral composition or the structure of interconnected struts of natural bone.[4–8] However, their utility are restricted by variable degradation rates, brittle or insufficient strength, and limited intrinsic osteoinductivity.[7–9] Improved autograft substitutes are needed to mimic bone hierarchy and surface topography, and match the performance of autografts to provide an optimal microenvironment for host stem cell recruitment and differentiation.[3,10]

During bone formation, nano-hydroxyapatites (nHAs) mainly deposit in the collagenous gap regions leading to staggered nanostructures (i.e., ≈67 nm *D*-periods, **Figure 1**a–c), which determine the biophysical properties of natural bone to constantly adapt to ever-changing mechanical needs and to support host stem cell differentiation, respectively.[1,11] However, this bone-like staggered hierarchy has rarely been reproduced, as its formation mechanism by energy change is far less understood.[12,13] The energy change underlying synthetic pathways in vitro is essentially different from that of the natural process in vivo. The latter is dominated by a dissipative self-assembly process, which is an energetically uphill

Prof. Y. Liu, M. Yu, Dr. Y. Wang, Dr. S. S. Jin, Z. X. Li, Dr. S. J. Cui, Dr. D. H. He, T. Zhang, Prof. Y. H. Zhou
Laboratory of Biomimetic Nanomaterials
Department of Orthodontics
Peking University School and Hospital of Stomatology
National Engineering Laboratory for Digital and Material Technology of Stomatology
Beijing Key Laboratory of Digital Stomatology
Beijing 100081, China
E-mail: orthoyan@bjmu.edu.cn; yanhengzhou@vip.163.com
Prof. D. Luo, Prof. T. Wang
Beijing National Laboratory for Molecular Sciences
Key Laboratory of Analytical Chemistry for Living Biosystems
Institute of Chemistry
The Chinese Academy of Sciences
Beijing 100190, China
E-mail: wangtie@iccas.ac.cn
Prof. D. Luo
College of New Energy and Materials
Beijing Key Laboratory of Biogas Upgrading Utilization
China University of Petroleum
Beijing 102249, China
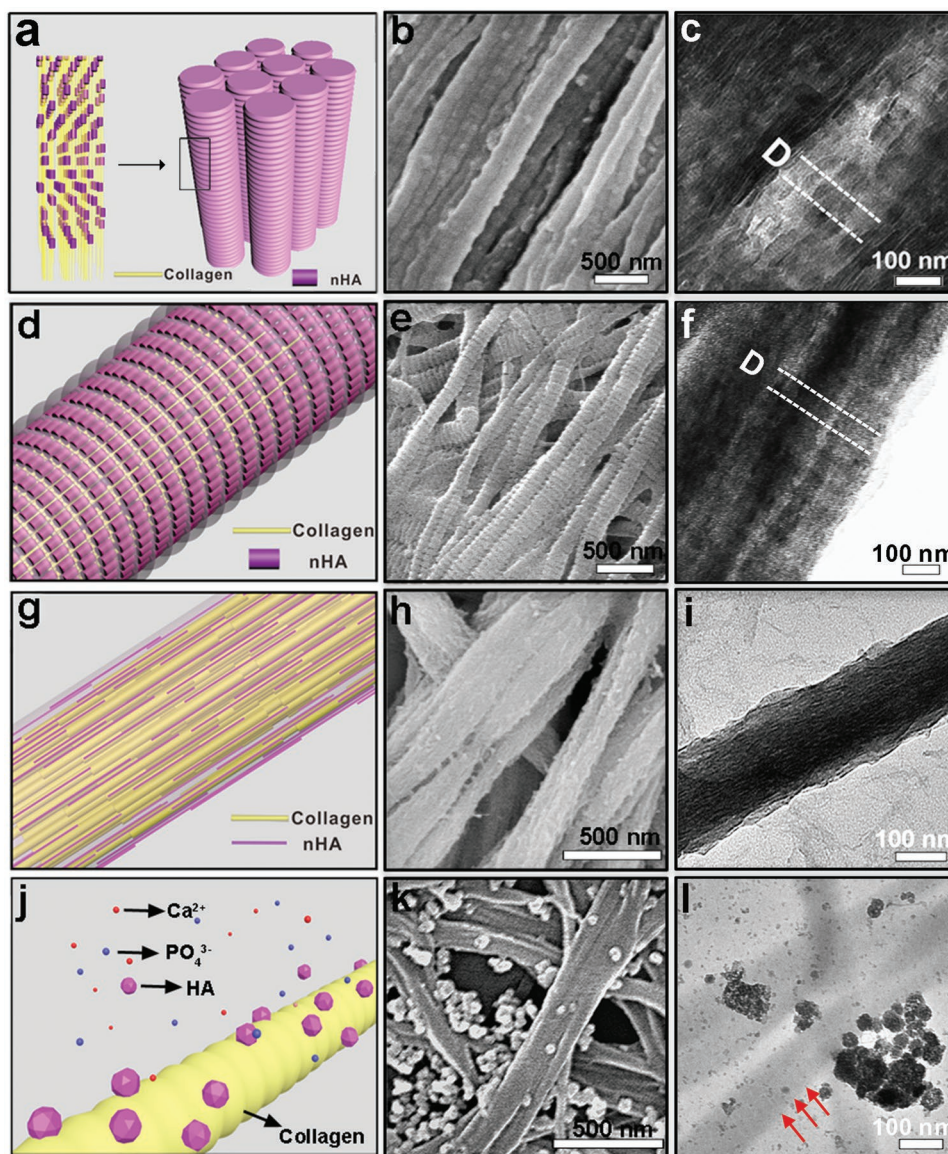
Figure 1. Fabrication and characterization of mineralized collagen prepared by PAA-Ca intermediates. a,d,g,j) Schematic illustration of formation of native bone, HIMC prepared by a PAA$_{2000}$-Ca intermediate, NIMC prepared by a PAA$_{72}$-Ca intermediate, and EMC prepared by a PAA$_{5000}$-Ca intermediate, respectively. b,e,h,k) Representative SEM images of native bone, HIMC, NIMC, and EMC, respectively. c,f,i,l) Representative unstained TEM images of native bone, HIMC, NIMC, and EMC, respectively. HIMC fibrils (diameter: 136.8 ± 36.9 nm) possess native bone-like *D*-periodic nanostructures, whereas minerals inside the NIMC fibrils (diameter: 162.2 ± 39.2 nm) destroy the hierarchical nanostructure of native collagen. In the EMC, HA clusters randomly arrange around the collagen fibrils (diameter: 83.9 ± 7.7 nm). *D* ≈ 67 nm. Arrows: unmineralized collagen fibril.

route relying on continuous consumption of bioenergy.[14] The selective transportation of calcium ions and crystallization of nHAs in the collagenous gap regions in vivo is regulated by enzymatic reactions accompanied by adenosine triphosphate hydrolysis.[15] On the contrary, the in vitro synthetic process is an energy downhill process driven by diminishing free energy.[16] Some in vitro models explaining intrafibrillar mineralization mechanisms have been proposed, including capillary force theory, size-exclusion theory, balance between osmotic equilibrium and electroneutrality.[17–19] However, these mechanisms are only applicable in explaining apatite nucleation in the intrafibrillar spaces, without elaborations on hierarchical structure formation. On the other hand, the relationship of the bone-like staggered hierarchy with the intrinsic osteoinductive potential of synthetic mineralized collagen is still unclear.[12,13] The aim of this study was to illustrate the mechanism of formation of staggered nanostructure from a thermodynamic point of view, and to provide a proof of concept for its clinical translation as an osteoinductive alternative to autografts with equal performance in the cell homing, osteogenic differentiation, and healing of a critical-sized bone defect.

2. Results and Discussion

2.1. Thermodynamic Control of Selective Transportation of Calcium Cations to Form Hierarchically Staggered Architecture

We designed a thermodynamically controlled approach to achieve precise synthesis of hierarchical intrafibrillarly mineralized collagen (HIMC). The self-assembly of HIMC involves two steps: (i) fabrication of a high-energy polyacrylic acid–calcium (PAA-Ca) intermediate, and (ii) hierarchical nanostructure, as a nadir point in the energy landscape, which was achieved through an energy descent pathway. The energy levels of PAA-Ca intermediates were capable to be regulated by adjusting PAA molecular weights, which trigger different mineralization modes, with distinct morphologies, mechanical properties, and biological functions. HIMC was fabricated using PAA with a molecular weight of 2000 and possessed staggered nanostructures with D-periods of 63.9 ± 3.3 nm light- and dark-contrast zones similar to the natural bone (Figure 1a–f). Scanning transmission electron microscopy (STEM) elemental mapping indicated the periodic distribution of Ca and P in the gap and overlap regions of HIMC with the Ca/P ratio of 1.58 ± 0.13, which is similar to that of natural bone (Figure S1, Supporting Information).[20] The mineral phase of HIMC was identified by X-ray diffraction, indicating the presence of nHAs (Figure S2, Supporting Information). When PAA$_{72}$-Ca was used as an intermediate, nonhierarchical intrafibrillarly mineralized collagen (NIMC) fibrils with clusters of short filaments were achieved (Figure 1g–i). Transmission electron microscopy (TEM) showed that minerals inside the NIMC fibrils destroyed the staggered nanostructure of native collagen, resulting in no obvious boundary in the gap and overlap regions. Furthermore, NIMC exhibited an irregular distribution of Ca and P but with a similar Ca/P ratio of ≈ 1.60 to HIMC (Figure S3, Supporting Information). When the energy downhill process started from PAA$_{5000}$-Ca, EMC fibrils formed, with nHA clusters randomly arranged around the collagen fibrils (Figure 1j–l).

The selective transportation of calcium ions and crystallization of nHAs in HIMC relies on competitive binding of calcium ions between PAA and collagen amino acids. The repetitive nature of the collagen amino acid sequences builds a hexagonal or quasihexagonal supramolecular structure containing periodic 40 nm gap and 27 nm overlap regions (Section 3.2 and Figure S4, Supporting Information).[21] Figure S5 (Supporting Information) details the amino acid sequences in each sub-band of gap and overlap regions. Aspartic acid (Asp) and glutamic acid (Glu), possessing specific calcium binding abilities, are described in Table S1 (Supporting Information). The binding capability of a calcium ion is directly proportional to the acidic amino acid amount based on the proposed fitted curve (Figure S6, Supporting Information). The average calcium binding capabilities of gap and overlap regions were evaluated, and the gap region was predominant (Tables S2 and S3, Supporting Information). Moreover, the gap region exhibited a packing density 20% smaller than that of the overlap region, providing more spatial binding sites for calcium cations. The Gibbs free energies of the Gap-Ca and Overlap-Ca formations can be estimated as follows (Section S3.3, Supporting Information)

$$Ca^{2+}_{(aq)} + Collagen_{(Gap/Overlap)} \rightarrow Ca_n\, Collagen_{(Gap/Overlap)}$$
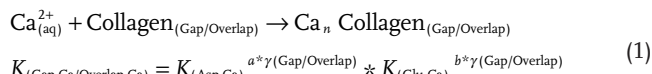
$$K_{(Gap\text{-}Ca/Overlap\text{-}Ca)} = K_{(Asp\text{-}Ca)}{}^{a*\gamma(Gap/Overlap)} * K_{(Glu\text{-}Ca)}{}^{b*\gamma(Gap/Overlap)} \tag{1}$$

$$\Delta G_{(Gap\text{-}Ca/Overlap\text{-}Ca)} = -RT\ln K_{(Gap\text{-}Ca/Overlap\text{-}Ca)}$$
$$+ RT\ln \frac{\left[Ca_n Collagen_{(Gap/Overlap)}\right]}{\left[Ca^{2+}_{(aq)}\right]^n \left[Collagen_{(Gap/Overlap)}\right]} \tag{2}$$

where a and b represent the contents of Asp and Glu in the gap and overlap regions, respectively; $K_{Asp\text{-}Ca}$ and $K_{Glu\text{-}Ca}$ are the calcium-binding constants of Asp and Glu;[22] γ is the accessibility of Asp or Glu while binding with calcium: 14.7% in overlap and 13.6% in the gap; and n indicates the total calcium binding number ($n = a*\gamma + b*\gamma$).

The competitive selection of calcium ions among PAA, overlap and gap regions is under thermodynamic control (Section S3.4, Supporting Information). At the appropriate molecular weight ($1720 < M_w < 2265$), in our case PAA$_{2000}$, the Gibbs free energy of PAA$_{2000}$-Ca was lower than that of Overlap-Ca but higher than that of Gap-Ca (**Figure 2**a,d). The free energy was at a minimum when the nucleation and growth of nHAs occurred in narrowly distributed gap regions, leading to HIMC. Low molecular weight of PAA$_{72}$ ($M_w < 1720$) increased the free energy of PAA$_{72}$-Ca; if the energy is higher than those of Overlap-Ca and Gap-Ca, the calcium binding sites uniformly distribute throughout the collagen, allowing the nHA nuclei to generate NIMC (Figure 2b). High molecular weight PAA$_{5000}$ ($M_w > 2265$) inhibited the release of the calcium cations to collagen fibrils; in this case, as PAA$_{5000}$-Ca had the lowest Gibbs free energy, which promoted EMC formation (Figure 2c). Once the calcium cations bind with the gap/overlap region, the chemical equilibrium between PAA-Ca, Gap-Ca, and Overlap-Ca is altered. Positively and negatively charged amino acids are attracted to each other, leading to overlap between the calcium adsorption layer and phosphate adsorption layer (Figure S7, Supporting Information). This, in turn, promotes nHA nucleation to form stable hierarchical structures.

PAA concentration is another important factor in regulating thermodynamics of mineralized collagen. During mineralization, collagen fibrils were exposed to a weakly alkaline solution with an appreciable amount of calcium cations and phosphate anions, which promoted formation of micrometer-sized HA crystals around collagen fibrils (Section S3.5 and Figure S8, Supporting Information). At zero or low (<0.0002 M) concentration of PAA$_{2000}$, HA crystallized around collagen fibrils, resulting in EMC. When the concentration increases to 0.0002 M, the free energy of the PAA$_{2000}$-Ca decreased exponentially to the threshold value, yielding pure PAA$_{2000}$-Ca intermediates (Figure 2e–h; Section S3.6 and Figure S9, Supporting Information). This results in a highly favorable thermodynamic situation, caused by the free energy of PAA$_{2000}$-Ca, which leads to intrafibrillar mineralization. These PAA$_{2000}$-Ca intermediates are sufficiently small to coassemble within collagen fibrils and form nHA nuclei with diameters of ≈ 2 nm (Figure S10, Supporting Information). Although PAA$_{2000}$ could avoid extrafibrillar mineralization, excessive PAA$_{2000}$ (>0.001 M) may
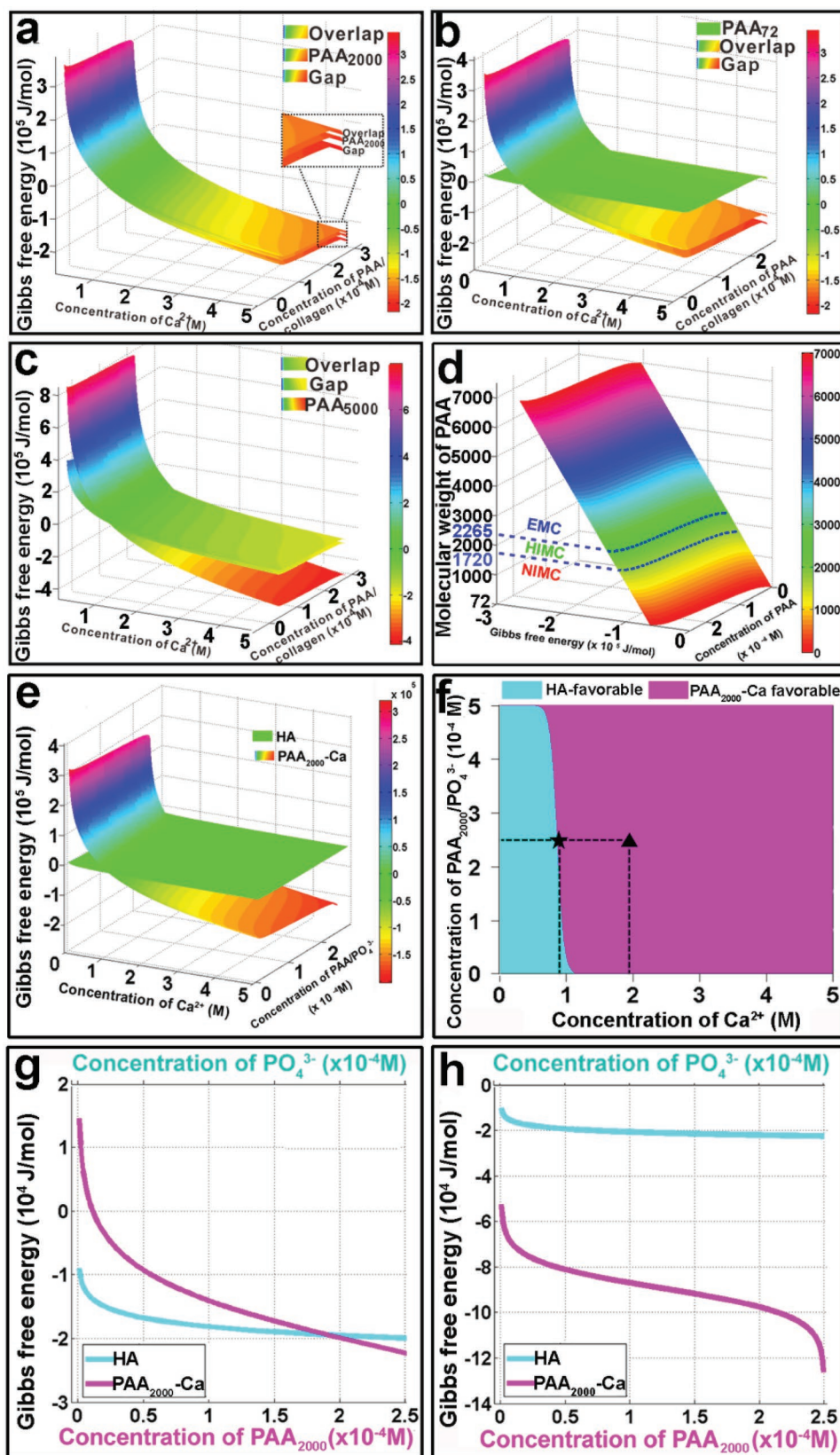
deplete free calcium ions and alter the dynamics of inorganic phase crystallization, delaying nHA nucleation (Figure S11, Supporting Information). From a thermodynamic perspective, HIMC formed only in a narrow range of molecular weights and restricted PAA$_{2000}$-Ca intermediate concentrations.

2.2. Cell-Homing Performance of Hierarchically Staggered Architecture

The natural bone healing process essentially involves the recruitment of progenitor stem cells to the wound site.[23] As the gold standard for bone repair, bone autografts have the natural bone hierarchical structure and create an optimal microenvironment to recruit host cells and direct functional regeneration. The elaborate HIMC under thermodynamic control possessing physicochemical properties and biocompatibility (Figure S12a, Supporting Information) highly consistent with natural bone is believed to behave similarly in cell-homing performance to autografts. Herein, to assess the intrinsic cell-homing capability in vitro, bone marrow mesenchymal stem cells (BMMSCs) were passed through the dialyzers filled by natural decellularized bone matrix (DCBM), HIMC, and NIMC without growth factors loading at 25 mL min^{-1} (**Figure 3**a). EMC was not included for its poor biocompatibility in the following experiments (Figure S12a, Supporting Information). After three cycles, the recruited cell number on HIMC was 212.87 ± 32.12 mm^{-3}, which was similar to that on DCBM with 210.11 ± 43.76 mm^{-3}, and much more than that on NIMC with 28.09 ± 14.99 mm^{-3} (Figure 3b). This phenomenon was further confirmed by the 3D confocal scanning, in which the cell density on DCBM and HIMC was much higher than that on NIMC (Figure 3c). By simulating blood circulation in vitro, we demonstrated the higher efficiency of cell homing on both HIMC (≈83.55%) and DCBM (≈82.47%) than that on NIMC (≈11.02%), indicating that HIMC, with a bone-like staggered architecture, offers a bone-specific microenvironment to home BMMSCs. In addition, scanning electron microscopy (SEM) revealed that the single BMMSC on DCBM and HIMC exhibited more cell pseudopodia, which were important intracellular cues in stimulating stem cell differentiation.[24]

2.3. Multidifferentiation Potential of Mesenchymal Stem Cells (MSCs) on HIMC

Next, we evaluated the osteoinductive potential of candidate autograft substitutes in vitro by studying osteogenesis of undifferentiated MSCs in contact with synthetic mineralized collagen. Biomaterials can *give* signals to cells via their nanostructural properties, in which nanometer-scale topography independently controls physical inputs to cells and regulates their shape, adhesion, and differentiation.[25,26] Here, we hypothesized that mineralized collagen prepared with a similar chemical composition but a different nanotopography influences cell fate by changing the covalent anchoring density of cells (**Figure 4**a). From atomic force microscopy (AFM) measurements, the surface of DCBM and HIMC followed an undulating topography with a periodic bisignate peak-dip shape and a large amplitude, whereas NIMC produced a relatively homogenous surface with a amplitude of 4.08 ± 2.31 nm, smaller than that of DCBM (14.18 ± 1.61 nm) and HIMC (14.35 ± 2.55 nm) (Figure 4b). The critical minimum scale of features required for cells to detect and interact with the surface is reported to be 8 nm;[26,27] as such, 100% of the surface area of NIMC fell within the fluctuation range for integrin. However, for DCBM and HIMC, the proportions of the surface topographies recognized by integrin receptors were reduced to 62.89 ± 3.86% and 62.08 ± 4.08%, respectively. The relationship between anchoring density and strength adhesion is given by

$$W = 48EI\Delta Z/L^3 \qquad (3)$$

where W is the force loaded onto the stem cell, E is Young's modulus, L is the distance between neighboring anchoring points, and I is the moment of inertia. This reduction of the anchoring density corresponds to an increase in the anchoring distance. As shown in Figure S13 (Supporting Information), the Young's modulus of HIMC ranging from 5.75 to 11.61 GPa was much higher than that of NIMC ranging from 5.49 to 8.56 GPa (Figure S13, Supporting Information). According to the formula, the mechanical feedback that cells sense on integrin ligation in HIMC (2.04 ± 0.41) was similar to that in DCBM (2.35 ± 0.40), and nearly a threefold decrease compared with that in NIMC, therefore showing a promotion in cell differentiation (Figure 4c).[26]

To test the hypothesis that stem cells respond to the mechanical feedback provided by mineralized collagen with different nanotopography, cell shape as an intracellular signal simulating cell differentiation[28] was assessed by immunostaining BMMSCs with F-actin (phalloidin) to label the cytoskeletal arrangement. After 24 h of culture, the BMMSCs on DCBM and HIMC had extensive, well-defined stress fibers that traversed throughout the cells, whereas limited axial stress fibers were distributed in the cell periphery on the homogeneous surface

Figure 2. Thermodynamical control of collagen mineralization process. a) Gibbs free energy among Gap-Ca, Overlap-Ca, and PAA$_{2000}$-Ca. The energy of PAA$_{2000}$-Ca is lower than that of Overlap-Ca but higher than that of Gap-Ca, allowing the nHA nuclei in narrowly distributed gap regions to form HIMC. b) Gibbs free energy among Gap-Ca, Overlap-Ca, and PAA$_{72}$-Ca. The energy of PAA$_{72}$-Ca is higher than those of Overlap-Ca and Gap-Ca, allowing the nHA nuclei throughout the collagen to generate NIMC. c) Gibbs free energy among Gap-Ca, Overlap-Ca, and PAA$_{5000}$-Ca. PAA$_{5000}$-Ca had the lowest Gibbs free energy, resulting in EMC formation. d) Working range of PAA molecular weight evaluated through Gibbs free energy. e) Comparison of Gibbs free energy between HA and PAA$_{2000}$-Ca. f) 2D energy watershed under different concentrations of PAA$_{2000}$ and calcium cations. The blue color represents that HA is more energy favorable; the purple color means that energy of PAA$_{2000}$-Ca is predominate. Star: the critical point for HA to PAA$_{2000}$-Ca phase transition at 4 h of mineralization; Triangle: PAA$_{2000}$-Ca phase favorable at 72 h of mineralization. g,h) Changes of Gibbs free energy under different concentrations of PAA at 4 h (0.9 M Ca^{2+}) and 72 h (1.95 M Ca^{2+}) of mineralization. The blue line stands for Gibbs free energy of HA and purple line means energy of PAA$_{2000}$-Ca.

1806445 (5 of 12)
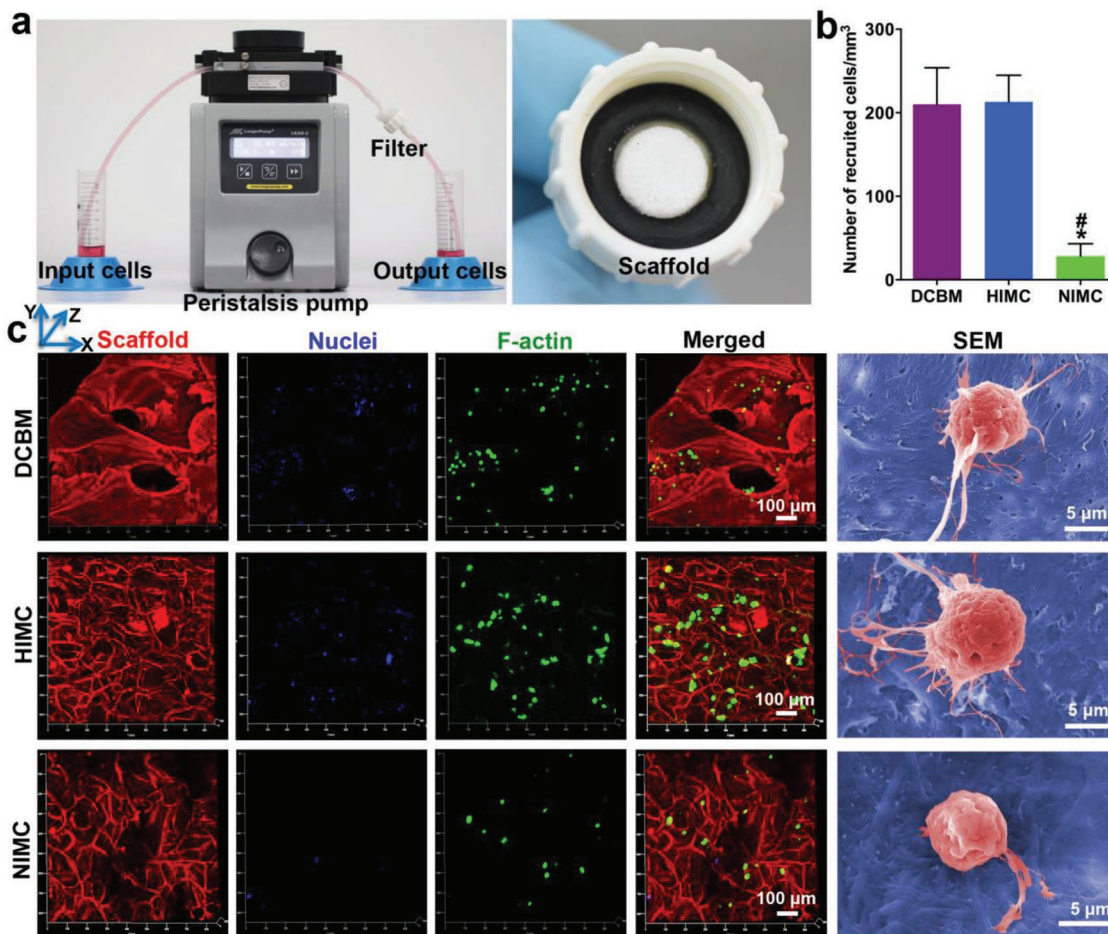
Figure 3. Cell-homing performance of mineralized collagen in fluid culture medium. a) Experiment setup showing filtration device during operation. b) Quantification of recruited cells in different scaffolds, showing enhanced cell-homing capability by hierarchical staggered nanostructure. c) Representative 3D immunofluorescence and SEM images of recruited cells in different scaffolds. Spherical cells with more pseudopodia are found in the DCBM and HIMC groups. *: $\alpha < 0.05$ versus DCBM; #: $\alpha < 0.05$ versus HIMC.

of NIMC. Furthermore, the morphology was altered for cells depending on surface nanotopography, where cells on surfaces with staggered nanostructure had highly branched, well-spread morphologies, and those on the homogeneous surface exhibited polarized morphologies and no spread (Figure 4d; Figure S12b, Supporting Information). The performance of cultured cells on mineralized collagen is consistent with that of recruited cells. Taken together, BMMSCs could *feel* the substrate topography and generate contractile forces against the substrate to create customized morphologies.[25] More pseudopodia, stress fiber formation, and the branched spreading morphology that provide more cell–cell contact area (Figure S14, Supporting Information), have emerged as important cues in guiding stem cell differentiation (Figure 4e).[24]

To explore multilineage differentiation capability, we assessed BMMSCs adhered to different substrates for markers associated with osteogenesis and angiogenesis without inductive supplements (Figure 4f,g and Figure S15, Supporting Information). A close correlation between cell morphology and lineage marker expression was evident. The highly branched BMMSCs on DCBM and HIMC exhibited high osteogenic

potential by strongly positive staining of runt-related transcription factor 2 (Runx2, early transcription factor required for osteoblastogenesis and bone formation) on day 7 and upregulated mRNA gene expression of Runx2 and osteocalcin (OCN, a late-stage marker of osteogenesis) on day 7 and 14. This finding is consistent with recent reports that osteogenic gene expression of stem cells on nanoscale rough surfaces is enhanced, and the branched morphology is also compatible with cell osteogenic differentiation.[24] The angiogenesis potential of BMMSCs on mineralized collagen was assessed by immunofluorescent staining of vascular endothelial growth factor (VEGF) and mRNA expression levels of VEGF and transforming growth factor beta 1 (TGFβ1). After 7 d of culture, the cells on DCBM and HIMC were strongly stained with VEGF (Figure 4f). The gene expression levels of VEGF and TGFβ1 in the DCBM and HIMC groups were similar, but much higher than those in the NIMC group on day 7 and 14 (Figure 4g). As a result of a positive feedback mechanism, the high expression of Runx2 could further enhance the VEGF secretion, which in turn stimulates an angiogenic response.[29] The osteogenic/angiogenic responses induced by the staggered architecture might

**ADVANCED
SCIENCE NEWS**
www.advancedsciencenews.com

**ADVANCED
FUNCTIONAL
MATERIALS**
www.afm-journal.de
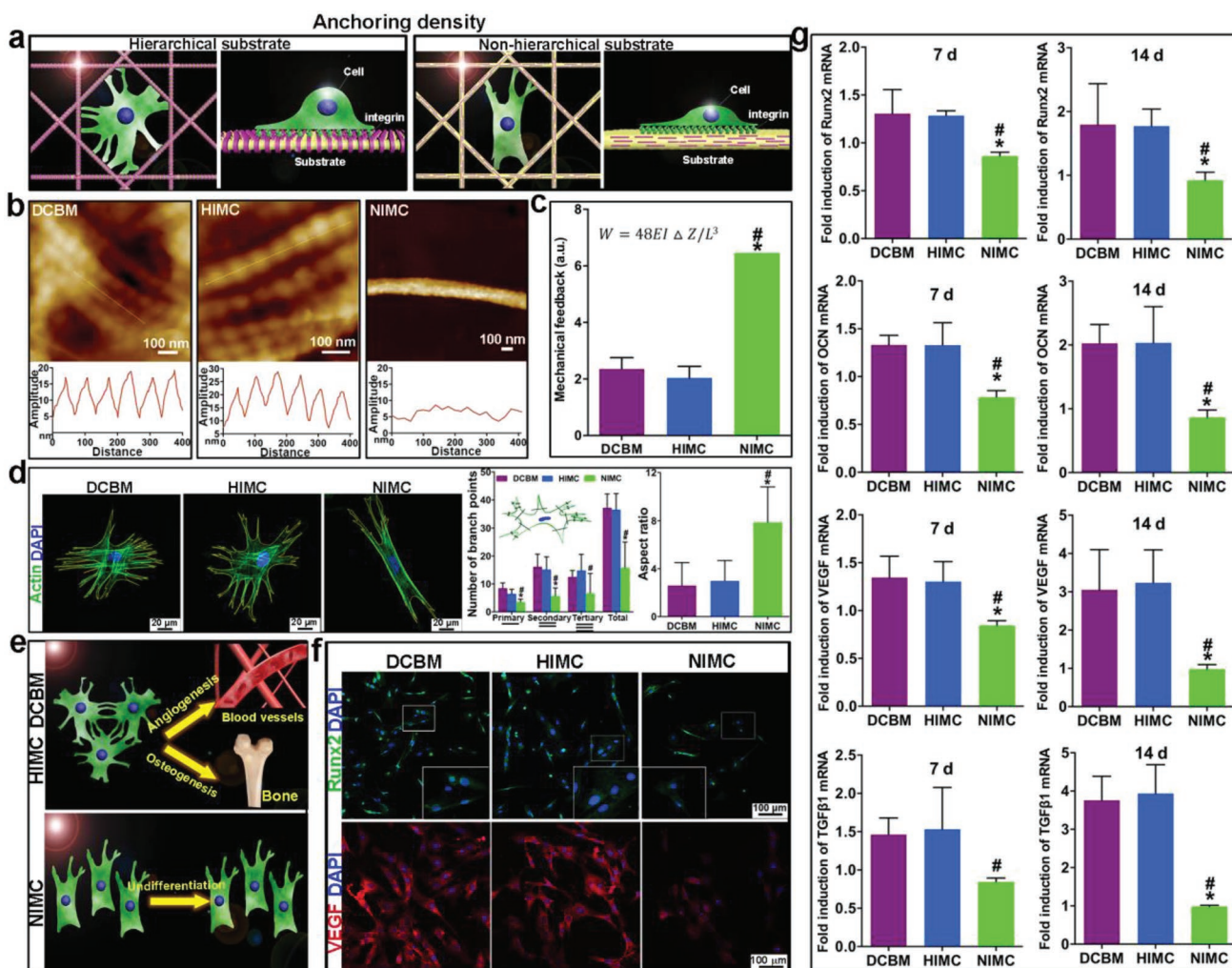
Figure 4. Stem cell differentiation on hierarchical and nonhierarchical substrates. a) Scheme of cell–scaffold interactions (yellow: collagen fibrils; purple: nHAs). b) AFM height images and corresponding cross-sectional analysis over six *D*-periods of DCBM, HIMC, and NIMC. c) Mechanical feedback of mineralized collagen with different nanotopography. d) Cell morphology, semiquantitation of cell branch points, and aspect ratio (green: actin filaments; blue: cell nuclei). e) Scheme of cell differentiation on different substrates. f) Immunofluorescence staining of Runx2 and VEGF on different substrates at 7 d. g) Relative mRNA expression levels of osteogenesis and angiogenesis related genes at 7 and 14 d. *: $\alpha < 0.05$ versus DCBM; #: $\alpha < 0.05$ versus HIMC.

be mediated by a PI3K/Akt signaling pathway, which plays an important role in bone and vessel formation.[30] BMMSCs, as a heterogeneous cell population, could produce Runx2 and VEGF, and therefore can potentially modulate osteogenesis and angiogenesis.[31] Herein, HIMC could *take* cell-secreted signals from the cell microenvironment, and thereby amplify cell expansion and the multidifferentiation potential.

2.4. Normal Architecture of Natural Bones with Bone Marrow Compartments Established by HIMC

While such in vitro tests give an indication of the potential osteoinductivity of HIMC, confirmation of in vivo bone formation is necessary for an osteoinductive alternative to bone autografts.[5] HIMC, by mimicking the in vivo cell-supporting niche with regard to its structural (Figure 1) and mechanical properties

(Figure S13, Supporting Information), is thought to coax niche cells into behaving similarly to their natural in vivo counterparts and therefore lead to structural and functional bone regeneration. To test this hypothesis, 3D porous collagen scaffolds with interconnected pores between 163 and 204 µm without exogenous cells and growth factors loading, were implanted into rat critical-sized mandibular bone defects (**Figure 5**a). DCBM with a pore size of 220.16 ± 54.12 µm was used as a positive control. Twelve weeks after implantation, the defects were almost entirely filled with bone structures, even in the defect center in the HIMC group, which was similar to the DCBM group. Limited bone formation was mainly restricted to the defect margins in the NIMC group. No obvious bone formation was observed in the untreated group, indicating a reliable animal model (Figure S16, Supporting Information). The neo-bone microstructure was examined by hematoxylin and eosin (HE) and Masson's trichrome staining (Figure 5b). An abundant amount

**ADVANCED
SCIENCE NEWS**
www.advancedsciencenews.com

**ADVANCED
FUNCTIONAL
MATERIALS**
www.afm-journal.de
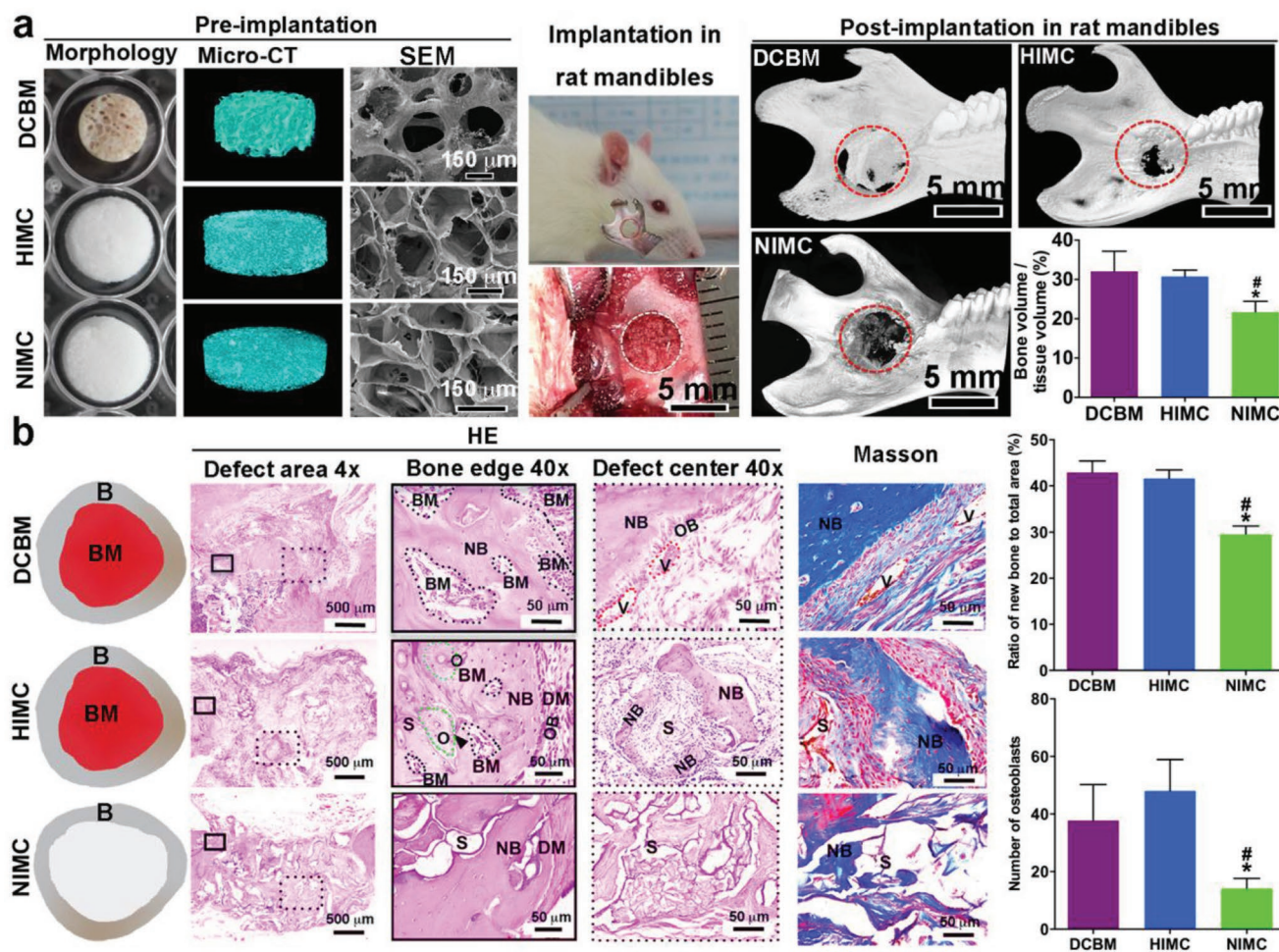
Figure 5. Normal architecture of natural bone with bone marrow compartments established by HIMC. a) Gross, micro-CT, and SEM morphology of different scaffolds before transplantation and 12 weeks post-transplantation in rat critical-sized mandibular bone defects (5 μm in diameter). DCBM with a pore size of 220.16 ± 54.12 μm was used as a positive control. HIMC and NIMC showed similar interconnected pores between 163 and 204 μm. b) Illustration of transverse plane, HE and Masson stainings, and semiquantitative analysis of engineered bones in rat mandibles. *: $\alpha < 0.05$ versus DCBM; #: $\alpha < 0.05$ versus HIMC. S: scaffold; NB: neo-bone; V: vessel; BM: bone marrow (green circles); OB: osteoblasts; DM: defect margin; B: bone.

of neo-bone with osteoblasts and bone marrow was regenerated by DCBM and HIMC, whereas only moderate neo-bone without bone marrow or vessel formation was noted in the NIMC group. A similar result was found in the minipig defect model, in which the engineered cranial bone by HIMC showed a completely normal architecture of natural bone with osteons and blood vessels, whereas limited newly formed bone and lots of residual scaffolds were observed in the HA group (Figure S17, Supporting Information). After 12 weeks of implantation, most of the scaffolds were degraded and remanent scaffold was similar to 6.75 ± 1.43% of HIMC and 6.49 ± 1.45% of NIMC. Furthermore, osteoclast-like cells were present in the engineered bones by DCBM and HIMC, as evident from the tartrate-resistant acid phosphatase (TRAP) assay (Figure S18, Supporting Information). The coexistence of osteoclast-like cells with osteoblasts implies potential remodeling of the engineered bone.[32] Taken together, HIMC shows a great regenerative capacity comparable to bone autografts, and the engineered bone by HIMC exhibits structural and functional characteristics similar to native bone organ with a marrow compartment (Figure S19, Supporting

Information) and a remodeling potential. These findings provide a highly relevant evidence to support the future clinical translation of HIMC.

Osteogenic cells are the critical functional unit in bone healing process. Current strategies for bone regeneration often require codelivery of scaffolding material and stem cells. However, isolation and expansion of stem cells is time-consuming and costly.[33] Therefore, no exogenous stem cells were loaded into the defect area in the present study. Here, the stem cell recruitment in vivo was assessed by staining the engineered bone for CD146, which has been believed as a common marker for MSCs.[34] Both immunofluorescence (**Figure 6**a) and immunohistochemical (Figure 6b) staining showed enhanced expression of CD146 in the engineered bones by DCBM and HIMC, indicating more MSC recruitment and greater differentiation potential of MSCs.

Bone defect healing is a dynamic progenitor cell-driven tissue morphogenetic process that requires coordinated osteogenesis and angiogenesis at the repair site.[35] To explore the complex interplay of autocrine and paracrine factors produced

**ADVANCED
SCIENCE NEWS**
www.advancedsciencenews.com

**ADVANCED
FUNCTIONAL
MATERIALS**
www.afm-journal.de
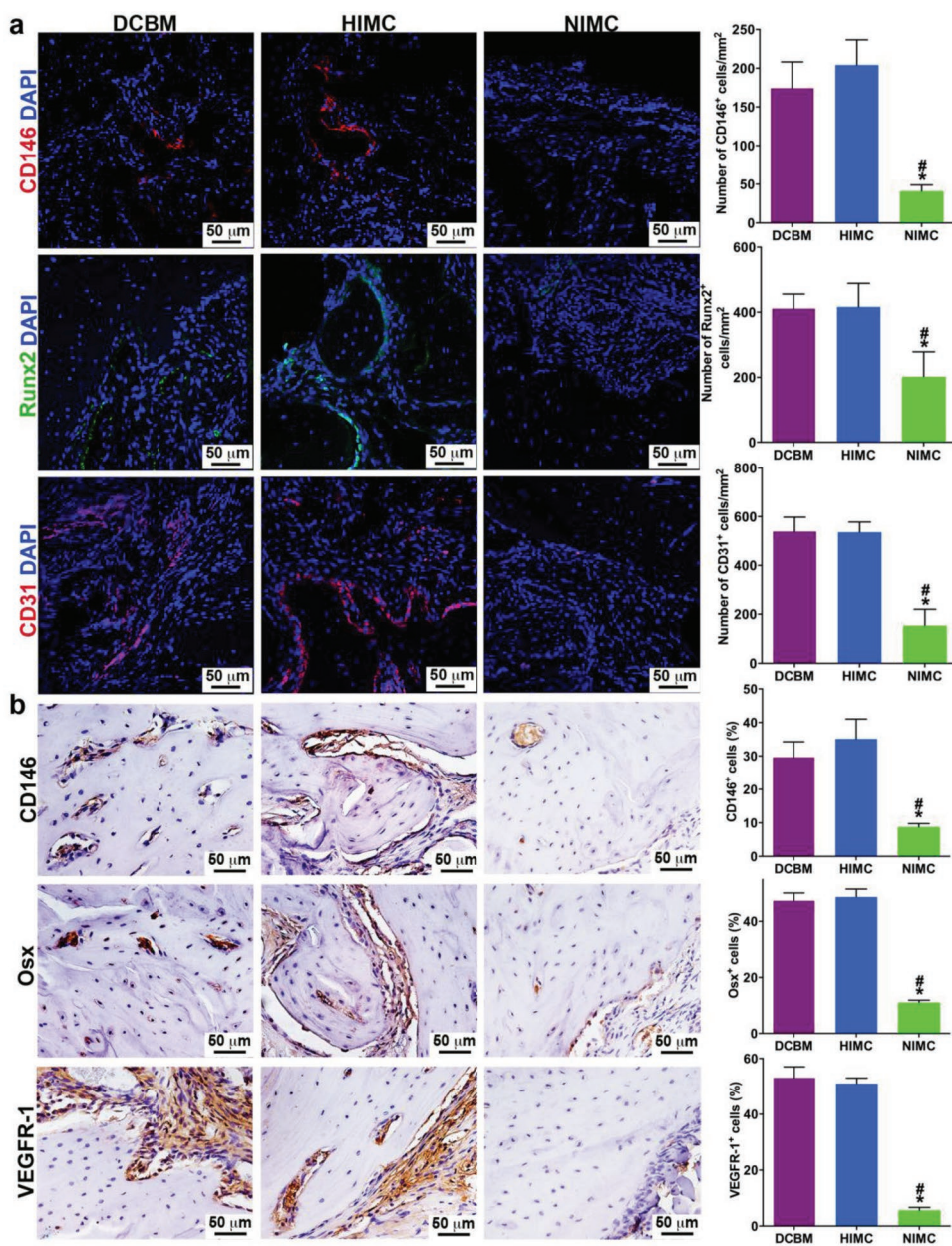
Figure 6. MSC recruitment, osteogenesis, and angiogenesis in the defect area. a) Representative immunofluorescence images of CD146, Runx2, and CD31 with quantification of positive cells. b) Representative immunohistochemical images of CD146, Osx, and VEGFR-1 with quantification of positive cells. *: $\alpha < 0.05$ versus DCBM; #: $\alpha < 0.05$ versus HIMC.

by osteoblasts, endothelial cells, and their precursors during bone defect healing, the engineered bone was further characterized for osteogenesis and angiogenesis by staining for related factors produced by osteoblasts and endothelial cells. Figure 6 showed the increased expressions of Runx2 and Osterix (Osx) of the engineered bones by DCBM and HIMC, reflecting a great osteoinductive potential of the two scaffolds. Although other cell types including preosteoblasts, pericyte-like cells, and endothelial cells may also express CD146, BMMSCs, with high expression level of CD146, are the major recruited cells during wound healing of natural bone and contributor cells to bone regeneration.[34,36] Accompanied with upregulated expressions

of osteoinductive markers Runx2 and Osx, we therefore speculate that the CD146 positive cells in the engineered bones are mainly BMMSCs. The mechanism of osteoinduction by DCBM and HIMC might be that materials first adsorb endogenous growth factors from the body fluids, which in turn facilitate the recruitment and homing of stem cells to form new bone.[37] This result also demonstrates that the intrinsic osteoinduction was not closely related to the chemistry of the materials, but the physical morphology of the biomaterial, especially nanostructure. The success of engineering functional bone also depends on the ability to vascularize the implantable tissue. This was confirmed by positive staining of CD31 and VEGFR-1

in the engineered bones by DCBM and HIMC, indicating the presence of vascular endothelial cells. The osteogenic/angiogenic differentiation of BMMSCs might also contribute to the osteogenesis and angiogenesis of the engineered bones by DCBM and HIMC. Taken together, the thermodynamically controlled self-assembly of HIMC matches the performance of autografts to provide an optimal microenvironment for host stem cell recruitment and differentiation, and to induce functional bone regeneration.

3. Conclusion

In summary, the natural, hierarchically staggered architecture was reproduced in vitro under thermodynamic control without enzyme catalysis or bioenergy consumption. The selective mineralization progress in collagenous gap regions was mediated by a high energy level of PAA-Ca intermediates with appropriate molecular weights and concentrations via an energetically downhill process. Without exogenous stem cells and growth factors loading, HIMC itself provided a favorable microenvironment for cell homing and multidifferentiation, and recruited host stem cells for bone regeneration with structural and functional characteristics similar to native bone organ with a marrow compartment and a remodeling potential. Together, this approach may represent a simple and straightforward strategy to fabricate hierarchical nanostructures for bone regeneration by avoiding the obstacles associated with cell transplantation and growth factors.

4. Experimental Section

Detailed methods are described in the Supporting Information.

Synthesis of Mineralized Collagen: Type I tropocollagen solution (Corning, 100 mg, 9.46 mg mL^{-1}, pH < 2) was continually injected into a dialysis flask (3500 Da), which was immersed in a mineralization solution containing 30 mL of calcium and magnesium-free solution (136.9 × 10^{-3} M NaCl, 2.7 × 10^{-3} M KCl, 8.3 × 10^{-3} M Na$_2$HPO$_4$, 1.25 × 10^{-3} M K$_2$HPO$_4$.3H$_2$O, and 3.08 × 10^{-3} M Na$_3$N, pH = 7.4) as a phosphate source, and the set type I white Portland cement (200 mg in 1 mL solution) as calcium source with performance of sustained and controlled release calcium cations.[12,13] HIMC was achieved by adding PAA with a molecular weight of 2000 (PAA$_{2000}$, 0.00025 M) to the mineralization solution to regulate apatite crystallization of HA. PAA$_{2000}$ could selectively bind calcium ions to form high-energy intermediates (PAA$_{2000}$-Ca), which regulate crystallization of HA in the gap regions of collagen fibrils. NIMC was obtained by using PAA with a molecular weight of 72 (PAA$_{72}$) and EMC was prepared by using PAA with a molecular weight of 5000 (PAA$_{5000}$) or without PAA in the mineralization solution. All the reactions were performed at 25 °C for one week in a moisture chamber.

Fabrication of 3D Porous Scaffolds: The acquired mineralized collagen was centrifuged, stirred to form a just-castable suspension, poured into a cylindrical-shaped or oblong-shaped mold and lyophilized to form 3D sponge-like collagen scaffolds. To stabilize the microstructure, the scaffolds were further cross-linked by using 1 wt% 1-ethyl-3-(3-dimethylaminopropyl)-carbodiimide (EDC) in 80% ethanol for 4 h, washed in 1 wt% glycine solution to remove the remanent EDC, and finally lyophilized for use.

Cytobiocompatibility of Scaffolds: Cytobiocompatibility of different scaffolds was determined using the cell-counting kit-8 (CCK-8). Rat BMMSCs identified[12] were seeded on different sterilized scaffolds on days 1, 3, and 7. Quantification was performed with a microplate reader according to the manufacturer's protocol. A calibration curve of BMMSCs was established to estimate the number of living cells from the absorbance index.

Cell-Homing Performance of Scaffolds In Vitro: For cell homing, mineralized collagen scaffolds with the same dimensions (5 mm diameter and 3 mm height) were fixed on a homemade pump device. Then, 30 mL of cell stock solution with 2 × 10^3 cells mL^{-1} was passed through the scaffolds at a flow rate of 25 mL min^{-1}. After three cycles, the scaffolds were removed from the device, fixed with 4% paraformaldehyde overnight and washed in phosphate buffered saline (PBS) for SEM and microscopy imaging. The cell recruitment number (N_r) of the scaffolds was calculated as follows

$$N_r = \frac{V \times (C_b - C_a)}{V_s}$$

where C_b and C_a represent the cell concentration in the stock solution before and after filtering, respectively, and V and V_s are the volumes of the stock solution and scaffolds, respectively.

Immunofluorescent Staining: To image recruited cell distribution, scaffolds were permeabilized with 0.1% Triton X-100 for 20 min and doubled-stained with type I collagen (1:200; sc-59772, Santa) and Alexa Fluor 488-Phalloidin (1:200; Thermo Fisher). To test the effect of the nanostructure of different mineralized collagen on cell morphology, BMMSCs were seeded on different sterilized substrates for 24 h, fixed with 3.7% formaldehyde in PBS for 10 min, stained with Alexa Fluor 488-phalloidin at 2 mg L^{-1} for 45 min. To investigate the osteogenic and angiogenic potential of different mineralized collagen, BMMSCs were seeded on different substrates for 7 d without induction, fixed with 3.7% formaldehyde in PBS for 10 min. Cell slides and tissue sections were incubated with primary antibodies such as CD146 (ab75769, Abcam), Runx2 (ab23981, Abcam), VEGF (ab1316, Abcam), and CD 31 (ab32457, Abcam) in the dilution 1:100 for 90 min at room temperature. Second antibodies labeled with Alexa Fluor 488 (1:200; Thermo Fisher) or Alexa Fluor 568 (1:200; Thermo Fisher) were used to bind primary antibodies for 1 h at room temperature. After washing with PBS, the cells and tissues were mounted with mounting media containing DAPI for nuclei staining and observed by a Zeiss LSM-710 scanning microscope. All animal procedures were approved by the Peking University Institutional Animal Care and Use Committee (LA2014218). The Image J software was applied to create cell outlines and analyze cell branch points, cell area, and aspect ratio. Three specimens were acquired in each group and six cells were randomly selected for each specimen (N = 18 cells).

Quantitative Real-Time Polymerase Chain Reaction (RT-PCR): To analyze the effect of the different scaffolds in the gene expression profile of BMMSCs, 2 × 10^5 cells were seeded per three scaffolds and cultured for 7 and 14 d in basic medium without induction. Total RNA was isolated using Trizol and the Nucleospin RNA isolation kit (Macherey-Nagel) according to the manufacturer's protocol. The synthesis of cDNA was performed using SuperScript III One-Step RT-PCR System with Platinum Taq High Fidelity (Invitrogen). Quantitative RT-PCR was applied to examine the expression of osteogenic differentiation gene makers Runx2 and OCN, and angiogenic differentiation gene makers VEGF and TGFβ1. Glycer-aldehyde 3-phosphate dehydrogenase (GAPDH) was used as the housekeeping gene. The primers designed by a primer premier 5.0 software and commercially synthesized were follows:

Rat-GAPGH GGTCGGTGTGAACGGATTTGG
GCCGTGGGTAGAGTCATACTGGAAC
Rat-Runx2 TGTGTGCCTCCAACCTGTGT
CTTTCCCCCTCAATTTGTGTCA
Rat-OCN GACCCTCTCTCTGCTCACTCTG
GCTCCAAGTCCATTGTTGAGG
Rat-VEGF TGCACTGGACCCTGGCTTTAC
CGGCAGTAGCTTCGCTGGTAG
Rat- TGFβ1 CACGATCATGTTGGACAACTGCTCC
CTTCAGCTCCACAGAGAAGAACTGC

Animal Surgery: To evaluate the bone regeneration potential of collagen scaffolds with different nanotopography, a critical size defect with 5 mm diameter was created in Sprague-Dawley rat mandible. The experimental protocols were approved by the Animal Use and Care Committee of Peking University (LA2014218). Twenty 6-week-old male rats were randomly divided into four groups: three groups were implanted with DCBM, HIMC, and NIMC scaffolds, and the negative control group was untreated. The wound was then closed in layers using 6-0 sutures.

As large animal studies may provide highly relevant evidence to support the future clinical applications of bone grafts, the HIMC scaffold (n = 4) was further implanted into critical-sized minipig cranial bone defects with ≈2 cm width × 3 cm length × 0.5 cm depth. The HA scaffold (n = 4) was used as a control. After 12 weeks of implantation, the minipigs were sacrificed via anesthesia overdose. The craniums were obtained from each group and fixed with 10% formalin in PBS. The protocols in this section were approved by the Animal Use and Care Committee of Peking University (LA2014218).

Micro-CT Analysis: Twelve weeks after operation, all the animals were euthanized by decapitation under deep anesthesia with a pentobarbital overdose (100 mg kg^{-1}). The mandibles were then fixed with 10% formalin in PBS. Serial images of fixed mandible tissue were acquired using a Bruker micro-CT system to assess new bone formation. 3D image reconstruction and bone volume calculation (60 < gray value < 255) were performed using the CTAn software (Bruker, Belgium).

Histochemical Staining of Engineered Bone: The fixed mandibles were decalcified in 10% EDTA for eight weeks. Samples were then embedded in paraffin and serial sections with 5 µm were prepared. Three randomly selected cross sections from each implant were stained with hematoxylin and eosin. Neo-bone formation was assessed by Masson's trichrome staining. To investigate whether osteoclast-like cells are present in the engineered bone tissue, the sections were stained with TRAP (Sigma-Aldrich). The stained slides were observed under a Zeiss light microscope.

Immunohistochemical Staining: Decalcified and rehydrated sections were prepared from the excised implants. Immunohistochemistry was performed with a two-step detection kit (Zhongshan Golden Bridge Biotechnology, Beijing, China). Tissue sections (N = 6) in each group were subjected to antigen retrieval using 0.125% trypsin and 20 µg mL^{-1} proteinase K, blocked with 5% bovine serum albumin and incubated overnight with antibodies against CD146 (1:100; ab75769, Abcam) for a stem cell surface marker, Osx (1:800; ab22552, Abcam) for an osteogenesis marker and VEGFR-1 for an angiogenesis (1:400; ab51872, Abcam). The sections were subsequently incubated with horseradish peroxidase-conjugated secondary antibodies, using diaminobenzidine (Zhongshan Golden Bridge Biotechnology, Beijing, China) as chromogen. The stained sections were imaged under a Zeiss light microscope.

Statistical Analysis: All the values generated in the cell and animal experiments were averaged and expressed as means ± standard deviation. The statistical differences were determined using one-way analysis of variance with Tukey's post-hoc test at $\alpha = 0.05$.

Supporting Information

Supporting Information is available from the Wiley Online Library or from the author.

Acknowledgements

Conflict of Interest

The authors declare no conflict of interest.

Keywords

[1] D. Taylor, J. G. Hazenberg, T. C. Lee, *Nat. Mater.* **2007**, *6*, 263.

[2] O. Faour, R. Dimitriou, C. A. Cousins, P. V. Giannoudis, *Injury* **2011**, *42*, S87.

[3] E. García-Gareta, M. J. Coathup, G. W. Blunn, *Bone* **2015**, *81*, 112.

[4] H. Yuan, H. Fernandes, P. Habibovic, J. de Boer, A. M. Barradas, A. de Ruiter, W. R. Walsh, C. A. van Blitterswijk, J. D. de Bruijn, *Proc. Natl. Acad. Sci. USA* **2010**, *107*, 13614.

[5] R. Z. Legeros, *Chem. Rev.* **2008**, *108*, 4742.

[6] X. Ren, D. Bischoff, D. W. Weisgerber, M. S. Lewis, V. Tu, D. T. Yamaguchi, T. A. Miller, B. A. Harley, J. C. Lee, *Biomaterials* **2015**, *50*, 107.

[7] B. Ye, X. Luo, Z. Li, C. Zhuang, L. Li, L. Lu, S. Ding, J. Tian, C. Zhou, *Mater. Sci. Eng., C* **2016**, *68*, 43.

[8] X. Liu, P. Wang, W. Chen, M. D. Weir, C. Bao, H. H. Xu, *Acta Biomater.* **2014**, *10*, 4484.

[9] F. J. O'Brien, *Mater. Today* **2011**, *14*, 88.

[10] S. Pina, J. M. Oliveira, R. L. Reis, *Adv. Mater.* **2015**, *27*, 1143.

[11] J. Aizenberg, J. Weaver, M. Thanawala, V. Sundar, D. Morse, P. Fratzl, *Science* **2005**, *309*, 275.

[12] Y. Liu, S. Liu, D. Luo, Z. J. Xue, X. A. Yang, L. Gu, Y. H. Zhou, T. Wang, *Adv. Mater.* **2016**, *28*, 8740.

[13] Y. Liu, D. Luo, X. X. Kou, X. D. Wang, F. R. Tay, Y. L. Sha, Y. H. Gan, Y. H. Zhou, *Adv. Funct. Mater.* **2013**, *23*, 1404.

[14] S. Maiti, I. Fortunati, C. Ferrante, P. Scrimin, L. J. Prins, *Nat. Chem.* **2016**, *8*, 725.

[15] Y. Nakano, W. N. Addison, M. T. Kaartinen, *Bone* **2007**, *41*, 549.

[16] E. Mattia, S. Otto, *Nat. Nanotechnol.* **2015**, *10*, 111.

[17] M. J. Olszta, X. Cheng, S. S. Jee, R. Kumar, Y. Y. Kim, M. J. Kaufman, E. P. Douglas, L. B. Gower, *Mater. Sci. Eng., R* **2007**, *58*, 77.

[18] P. A. Price, D. Toroian, J. E. Lim, *J. Biol. Chem.* **2009**, *284*, 17092.

[19] L. N. Niu, S. E. Jee, K. Jiao, L. Tonggu, M. Li, L. Wang, Y. D. Yang, J. H. Bian, L. Breschi, S. S. Jang, J. H. Chen, D. H. Pashley, F. R. Tay, *Nat. Mater.* **2017**, *16*, 370.

[20] B. Alexander, T. L. Daulton, G. M. Genin, J. Lipner, J. D. Pasteris, B. Wopenka, S. Thomopoulos, *J. R. Soc., Interface* **2012**, *9*, 1774.

[21] S. M. Sweeney, J. P. Orgel, A. Fertala, J. D. McAuliffe, K. R. Turner, G. A. Di Lullo, S. Chen, O. Antipova, S. Perumal, L. Ala-Kokkog, A. Forlinoi, W. A. Cabral, A. M. Barnes, J. C. Marini, J. D. San Antonioe, *J. Biol. Chem.* **2008**, *283*, 21187.

[22] G. A. Di Lullo, S. M. Sweeney, J. Korkko, L. Ala-Kokko, J. D. San Antonio, *J. Biol. Chem.* **2002**, *277*, 4223.

[23] E. L. Fong, C. K. Chan, S. B. Goodman, *Biomaterials* **2011**, *32*, 395.

[24] W. Liu, Y. Wei, X. Zhang, M. Xu, X. Yang, X. Deng, *ACS Nano* **2013**, *7*, 6928.

[25] W. L. Murphy, T. C. McDevitt, A. J. Engler, *Nat. Mater.* **2014**, *13*, 547.

[26] B. Trappmann, J. E. Gautrot, J. T. Connelly, D. G. Strange, Y. Li, M. L. Oyen, M. A. C. Stuart, H. Boehm, B. Li, V. Vogel, J. P. Spatz, F. M. Watt, W. T. S. Huck, *Nat. Mater.* **2012**, *11*, 642.

[27] L. E. McNamara, T. Sjöström, K. Seunarine, R. D. Meek, B. Su, M. J. Dalby, *J. Tissue Eng.* **2014**, *5*, 204173141453617.

[28] K. A. Kilian, B. Bugarija, B. T. Lahn, M. Mrksich, *Proc. Natl. Acad. Sci. USA* **2010**, *107*, 4872.

[29] Y. Zhou, X. Guan, M. Yu, X. Wang, W. Zhu, C. Wang, M. Yu, H. Wang, *Biotechnol. J.* **2014**, *9*, 944.

[30] C. Wang, K. Lin, J. Chang, J. Sun, *Biomaterials* **2013**, *34*, 64.

[31] D. Kaigler, P. H. Krebsbach, P. J. Polverini, D. J. Mooney, *Tissue Eng.* **2003**, *9*, 95.

[32] Y. R. Shih, H. Kang, V. Rao, Y. J. Chiu, S. K. Kwon, S. Varghese, *Proc. Natl. Acad. Sci. USA* **2017**, *114*, 5419.

[33] X. Ren, V. Tu, D. Bischoff, D. W. Weisgerber, M. S. Lewis, D. T. Yamaguchi, T. A. Miller, B. A. Harley, J. C. Lee, *Biomaterials* **2016**, *89*, 67.

[34] G. A. Pilz, C. Ulrich, M. Ruh, H. Abele, R. Schäfer, T. Kluba, H. J. Bühring, B. Rolauffs, W. K. Aicher, *Stem Cells Dev.* **2011**, *20*, 635.

[35] X. Hu, P. Zhang, Z. Xu, H. Chen, X. Xie, *J. Cell. Biochem.* **2013**, *114*, 2729.

[36] L. H. Chiu, W. F. Lai, S. F. Chang, C. C. Wong, C. Y. Fan, C. L. Fang, Y. H. Tsai, *Biomaterials* **2014**, *35*, 2680.

[37] G. Song, P. Habibovic, C. Bao, J. Hu, C. A. van Blitterswijk, H. Yuan, W. Chen, H. H. Xu, *Biomaterials* **2013**, *34*, 2167.